



ELSEVIER

Available online at [www.sciencedirect.com](http://www.sciencedirect.com)

SCIENCE @ DIRECT®

Journal of Magnetism and Magnetic Materials 293 (2005) 924–937

Journal of  
magnetism  
and  
magnetic  
materials

[www.elsevier.com/locate/jmmm](http://www.elsevier.com/locate/jmmm)

# TEM-characterization of magnetic samarium- and cobalt-rich-nanocrystals formed in hexagonal SiC

Johannes Biskupek<sup>a,\*</sup>, Ute Kaiser<sup>b,1</sup>, Hannes Lichte<sup>c</sup>, Andreas Lenk<sup>c</sup>,  
Thomas Gemming<sup>d</sup>, Gunnar Pasold<sup>a</sup>, Wolfgang Witthuhn<sup>a</sup>

<sup>a</sup>*Institute of Solid State Physics, Friedrich Schiller University Jena, Helmholtzweg 5, Max-Wien-Platz 1, D-7743 Jena, Germany*

<sup>b</sup>*Center of Microstructure and Nanotechnologies, TU Ilmenau, Kirchhoffstraße 1, D-98693 Ilmenau, Germany*

<sup>c</sup>*Institute of Structure Physics, Technical University Dresden, D-01069 Dresden, Germany*

<sup>d</sup>*Leibniz Institute for Solid State and Materials Research, Helmholtzstraße 20, D-01069 Dresden, Germany*

Received 18 October 2004; received in revised form 22 November 2004

Available online 25 December 2004

## Abstract

Using analytical transmission electron microscopy techniques, nanocrystals embedded in 4H-SiC are studied which formed after high dose samarium (Sm), cobalt (Co), and Sm-and-Co-ion implantations and annealing. SmSi<sub>2</sub>, Sm<sub>5</sub>C<sub>2</sub>, Co<sub>2</sub>Si and SmCo-rich nanocrystals have been identified in terms of their crystallography, shape, strain, size, and orientation relationship to the matrix. It is shown, moreover, that cluster creations of foreign atoms (nanocrystals) and of vacancies (voids) are connected and their sizes increase with implantation dose. Carbon onions surrounding the nanocrystals have been found and this carbon excess has been interpreted as a consequence of preferred formation of foreign atom-silicide nanocrystals. For the case of Co implanted 4H-SiC, Lorentz microscopy has been applied revealing both non-magnetic and single-domain ferromagnetic nanocrystals.

© 2004 Elsevier B.V. All rights reserved.

PACS: 36.40.Cg; 75.75.+a; 68.37.Lp

Keywords: Magnetic nanocrystals; SiC; Ion implantation; HRTEM; EELS/EDX-STEM; Electron holography

## 1. Introduction

SiC, a wide band gap semiconductor with outstanding electronic, optical, and mechanical properties (e.g. [1]), is also promising for applications in nanotechnology. There is considerable interest in the creation of ferromagnetic nanocrystals

\*Corresponding author. Tel.: +49 731 50 22930; fax: +49 731 50 22958.

E-mail address: [biskupek@pinet.uni-jena.de](mailto:biskupek@pinet.uni-jena.de) (J. Biskupek).

<sup>1</sup>Now at Electron Microscopy Group of Materials Science, University Ulm, Albert-Einstein-Allee 11, D-89069 Ulm, Germany.

embedded in SiC enabling the development of new devices for data information storage and high sensitive magnetic sensors [2,3]. Nanocrystals of the rare earth element Sm may be promising candidates because of its high magnetic susceptibility and magnetic anisotropy [4,5]. Even better hard-magnetic properties may be expected if the nanocrystals are created from alloys of Sm-and-Co [6]. But not only pure Sm-and-Co alloys promise magnetic properties: there are experimental studies on magnetic properties of bulk metal-carbides synthesized from graphite and rare earth elements like Sm [7]. However, properties of materials can be modified significantly if they are manipulated at the nanometer scale [8] and nanocrystals may differ from their bulk in terms of magnetic anisotropy, magneto-resistance, Curie-temperatures, and susceptibility [6,9]. Therefore careful characterization on the nanometer scale is required. Theoretical studies propose ferromagnetism for transitional metal-doped SiC [10,11] with impurity concentrations above 3%. The integral magnetic properties of Fe-, Ni-, and Mn-implanted SiC were experimentally investigated [12] showing ferromagnetism after a maximum impurity concentration of 5% (dose  $5 \times 10^{16} \text{ cm}^{-2}$ ). However, corresponding transmission electron microscopy (TEM)-studies did not reveal precipitates. Magnetic and electric properties of nanostructures can be studied by electron holography on Lorentz-microscopes after subsequent reconstruction of the phase images, which contain the electrical and magnetic information [13]. To the best of our knowledge, there are no reports about magnetic nanocrystals in SiC.

There is a wide range of theoretical studies [14–18] about the growth and formation mechanism of defect accumulations (foreign and host atoms, vacancies, interstitial loops, etc.) due to ion implantation in SiC. They suggest that number and sizes of the defect clusters are a function of the implantation dose.

Recently, nanocrystal formation in SiC after high dose ion implantation ( $\text{Al}^+$ ,  $\text{Si}^+$ ,  $\text{Ge}^+$ , and  $\text{Er}^+$ ) and annealing has been intensively studied [19–25] with the result that now it is confirmed that the nanocrystals start to grow at extended defects as wide interstitial loops [23,25]. Except the case of Al ion implantation, nanocrystals have not been

formed of the pure foreign atom material but of the foreign atom silicide ( $\text{GeSi}$ ,  $\text{ErSi}_2$ ). The question about the location of the excess Carbon (as Si from the SiC matrix was used to form the nanocrystal) remained unsolved. Voids after high dose ion implantation and annealing have been observed [26], however, their creation mechanism and relation to precipitate formation was not discussed so far.

In this work we report about the formation and characterization of nanocrystals formed in 4H-SiC after Sm, Co or Sm-and-Co-ion implantation and subsequent annealing.

## 2. Experimental

The ion energies of Co-, Sm-, and Co/Sm-ions were chosen such that after implantation always the maximum concentration of foreign atoms occurs in a depth of about 100 nm inside the SiC-matrix using TRIM calculations [27]. To avoid channelling the 4H-SiC was tilted by  $6^\circ$  to  $8^\circ$  away from the exact crystallographic direction.  $10^{17} \text{ cm}^{-2}$  200 keV  $\text{Co}^+$  ions,  $10^{16} \text{ cm}^{-2}$  400 keV  $\text{Sm}^+$  ions respectively,  $2 \times 10^{15} \text{ cm}^{-2}$  400 keV Sm ions and  $8 \times 10^{15} \text{ cm}^{-2}$  200 keV Co ions have been implanted into 4H-SiC. All ion-implantation experiments were carried out at high temperatures ( $700^\circ\text{C}$ ) followed by rapid thermal annealing for 120 s at  $1600^\circ\text{C}$  under a protective gas atmosphere at 200 mbar. (For more details to the implantation procedures see [28].)

Thin TEM foils were prepared for investigation in cross-sectional and plane-view geometries using standard techniques including mechanical polishing and low-angle argon thinning [29].

TEM was carried out using a JEOL JEM-3010 microscope operating at 300 kV, equipped with a  $\text{LaB}_6$  cathode applying high-resolution (HR) and high angle centred dark-field (HACDF) [30] imaging, and energy dispersive X-ray spectroscopy (EDX). A FEI Tecnai F30 microscope operating at 300 kV equipped with a field emission gun was used to apply high resolution EELS and EDX-spectroscopy together with high angle annular dark-field (HAADF) imaging. Electron holography was carried out using a Philips CM200 FEG

microscope operating at 200 kV equipped with a field emission gun, a Möllenstedt biprism and a Lorentz-lens operating in Lorentz-mode (objective lens switched off, Lorentz-lens active). Phase reconstruction of holograms has been carried out with the HoloWorks Package for Gatan Digital Micrograph [31].

The lattice parameters of the nanocrystals have been measured with the reciprocal space method [32–34] using the 0004-SiC-reflection ( $d = 0.2521$  nm) as calibration standard. The 1-100-SiC reflection has been measured to check if the matrix is strained around the nanocrystal (see details in Ref. [35]). The result is visualized in a two-dimensional lattice bending plot. The accuracy of lattice parameter determination of nanocrystal reflections reaches up to  $\Delta d/d = 0.005$  [35].

HRTEM images have been calculated using the multislice programme Musli [36] enabling the simulation of very large supercells. Nanocrystal models of different crystal structure, size, and shape have been embedded into a 4H-SiC matrix (approximately  $7 \text{ nm} \times 7 \text{ nm} \times 7 \text{ nm}$ , 35 000 atoms). This was done by preparing a [100]-oriented starting model and then tilting and cutting to the desired orientation and shape of the nanocrystal and finally placing it into the matrix while removing the atoms of the matrix (see details in Ref. [37]). The image calculation parameter were: defocus  $-64$  nm, aperture radius  $6 \text{ nm}^{-1}$ , focus spread 5.0 nm, convergence angle 0.5 mrad, vibrations 0.1 nm.

Measurements of the integral magnetic anisotropy were carried out using a torque magnetometer at room temperature. The pure 4H-SiC crystal was measured to eliminate diamagnetic matrix effects.

### 3. Results and discussion

#### 3.1. Samarium-implantation

Cross-sectional TEM investigations showed that after Sm (dose  $10^{16} \text{ cm}^{-2}$ ) implantation and annealing at  $1600^\circ\text{C}$ , as after Er and Ge ion implantation (see e.g. Ref. [25]), nanocrystals have been formed within 4H-SiC. A collection of

HRTEM images of typical different nanocrystals together with their corresponding diffractograms is shown in Fig. 1. The evaluation of the nanocrystals lattice parameters showed that in general samarium-silicide  $\text{SmSi}_2$  (space group  $I4_1/amd$ ) has been formed however a few nanocrystals could be identified as the samarium-carbide  $\text{Sm}_5\text{C}_2$  (space group  $Fm-3m$ ). It was found that the  $\text{SmSi}_2$  nanocrystals are unstrained within an unstrained matrix (analogue to the  $\text{ErSi}_2$  nanocrystals in 4H-SiC [25]) as is visualized in Fig. 1d–e by the lattice bending maps. (For the calculation of the maps the 1-100-reflection of 4H-SiC has been used (see 2. Experimental). It was found moreover that the  $\text{SmSi}_2$  nanocrystals appear in two different orientation relationships (type 1a and b) to the 4H-SiC matrix.

- Type 1a:  $020_{\text{SmSi}_2} // 0004_{\text{SiC}}$  and  $004_{\text{SmSi}_2} // 1-100_{\text{SiC}}$ ; and  $100_{\text{SmSi}_2} // 11-20_{\text{SiC}}$  (Fig. 1a,g).
- Type 1b:  $112_{\text{SmSi}_2} // 0004_{\text{SiC}}$  and  $100_{\text{SmSi}_2} // 11-20_{\text{SiC}}$  (Fig. 1b,h).
- Type 2:  $110_{\text{Sm}_5\text{C}_2} // 11-20_{\text{SiC}}$  (Fig. 1c,i).

Nanocrystals of type 1a ( $\text{SmSi}_2$ ) show the same hill-like shape and orientation as previously characterized  $\text{ErSi}_2$ -nanocrystals (see Ref. [25]). In contrast, type 1b nanocrystals, appear faceted always. In analogy to the formation of facets studied for the case of GeSi nanocrystals by molecular dynamics (MD) (see Refs. [24,37]), we conclude that the appearance of the facets of type 1b nanocrystals is connected to the force of the nanocrystal-matrix system to minimize the interface energy between nanocrystal and matrix (the verification of this statement is not possible up to now since there is no valid MD-potential for the system Sm-Si-C).

Nanocrystals of type 2 ( $\text{Sm}_5\text{C}_2$ ) are spherical shaped and are found to be tilted at different angles around the  $\langle 110 \rangle$  zone axis. The latter property may be connected (in analogy to our earlier MD studies [24]) to the small size and round shape. It can be seen from the lattice bending map (Fig. 1f) that the matrix is strained while the nanocrystal itself was found to be unstrained.

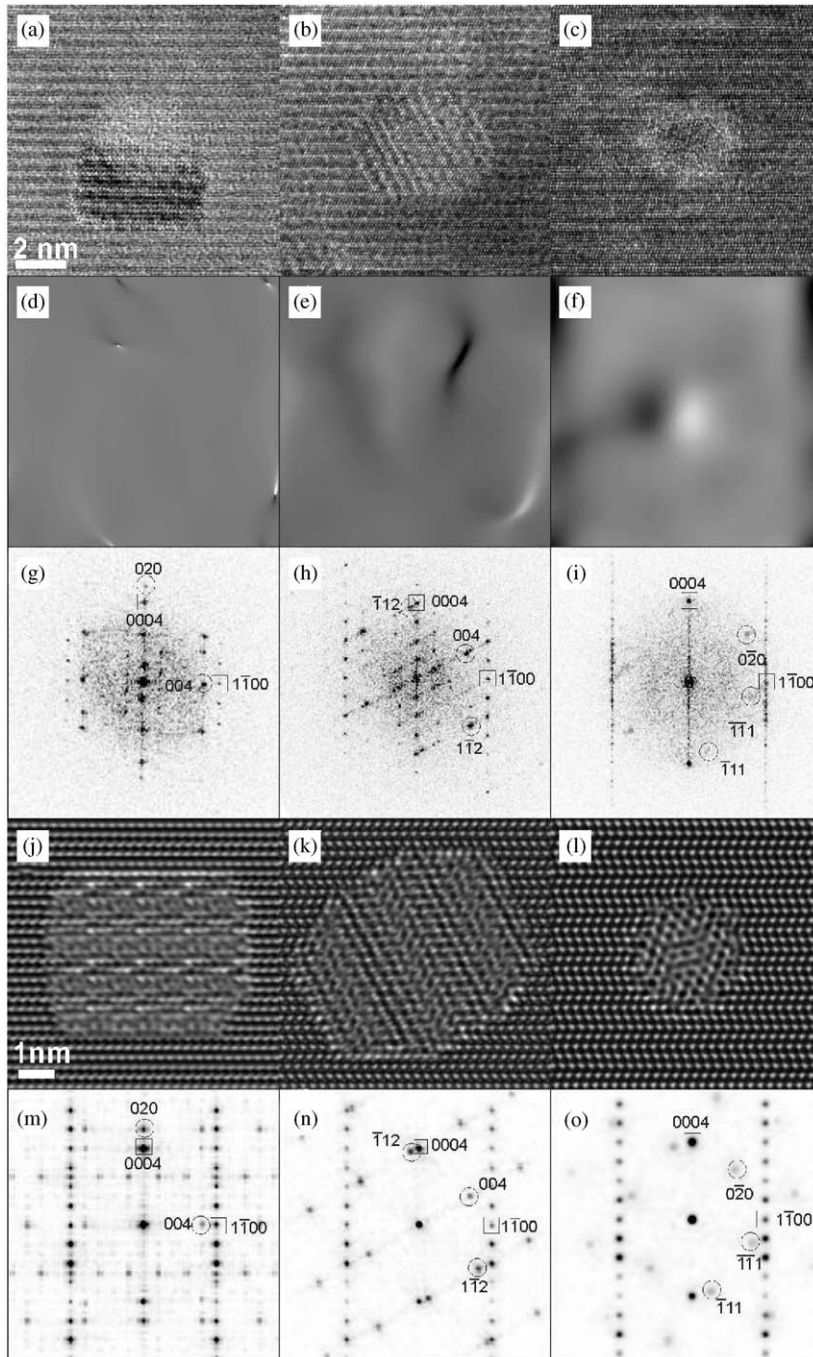


Fig. 1. Three typical types of nanocrystals created in 4H-SiC after Sm-ion implantation and annealing viewed along the  $[11\bar{2}0]$ -4H-SiC direction; experimental HRTEM images (a–c) corresponding lattice banding maps (d–f), diffractograms (g–i) and corresponding calculations: HRTEM images (j–l) and diffraction patterns (m–o) for  $[1\bar{1}0]$ -SmSi<sub>2</sub>-nanocrystal (a,d,g,j,m),  $[1\bar{1}0]$ -SmSi<sub>2</sub>-nanocrystal (b,e,h,k,n) and  $[1\bar{1}0]$ -Sm<sub>5</sub>Co<sub>2</sub>-nanocrystal (c,f,i,l,o). Reflections of the nanocrystals are encircled, reflections of the 4H-SiC matrix are boxed.

Pure crystalline Sm nanocrystals (space group R-3m) could not be identified yet. It should be noted that in thin specimen areas the nanocrystals were always found to be surrounded by a thin layer of amorphous material.

The last two rows of Fig. 1 show calculated HRTEM images of corresponding matrix-nanocrystal models. When comparing the experimental and calculated images (Fig. 1a–c, g–o) it is seen that the main HRTEM image details could be reproduced.

### 3.2. Cobalt implantation

As in the Sm-case, nanocrystals have been formed after Co (dose  $10^{17} \text{ cm}^{-2}$ ) ion implantation into 4H-SiC and subsequent annealing. Figs. 2a,c and 3a, respectively 3b show the embedded nanocrystal in cross-sectional respectively plane-view. Small  $\text{Co}_2\text{Si}$  nanocrystals were found to grow in a row near the specimen surface in two different orientation relationships to the 4H-SiC matrix, which were different from the Sm-case:

- Type 1:  $101_{\text{NC}}//11-20_{\text{SiC}}$  and  $020_{\text{NC}}//0004_{\text{SiC}}$  (Fig 2a, d).

- Type 2:  $100_{\text{NC}}//11-20_{\text{SiC}}$  and  $020_{\text{NC}}//0004_{\text{SiC}}$  (Fig 2c, f).

The HRTEM image calculation of the relevant embedded  $\text{Co}_2\text{Si}$  nanocrystal and the corresponding diffractograms (Fig. 2b and e) show that main HRTEM image details are well reproduced, confirming the existence of  $\text{Co}_2\text{Si}$  (space group Pnma) nanocrystals.

However, not only small (4–8 nm) nanocrystals near the surface have been formed but also significantly larger ones (reaching 40 nm) (see Fig. 3a and 9c) in the depth of maximal Co content. Selected area electron diffraction on some of these large nanocrystals showed reflections, which may fit to pure Co; however this result was not verified by HRTEM-experiments, due to a too complex lattice plane structure of the images (e.g. Fig. 9c).

The wider range of nanocrystal sizes, compared to the case of Sm-ion implantation, can be addressed to the higher (factor of 10) implantation dose. This is in agreement with theoretical predictions about the growth of clusters as a function of dose [18]. Small  $\text{Co}_2\text{Si}$  and  $\text{SmSi}_2$  nanocrystals,

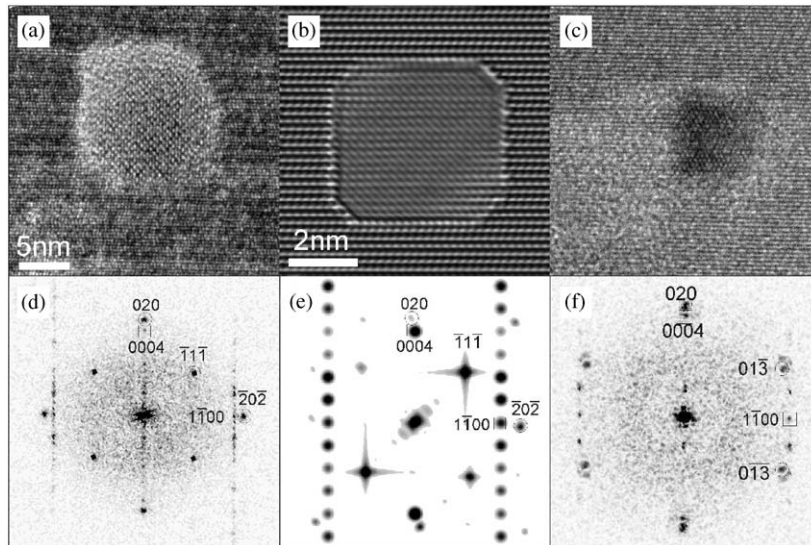


Fig. 2. HRTEM images of  $\text{Co}_2\text{Si}$ -nanocrystals in 4H-SiC created after Co-ion implantation and annealing viewed along  $[11-20]$  4H-SiC; experimental images (a, c) and the corresponding diffractograms (d, f); calculated image (b) and calculated diffraction pattern (e, the asymmetries of intensities are caused by inaccuracies during the tilting and embedding processes (see 2. Experimental)). Reflections of nanocrystals are encircled, reflections of 4H-SiC are boxed.

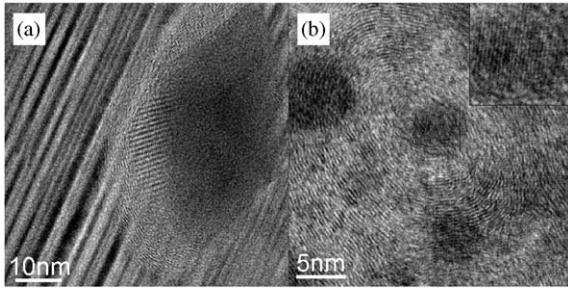


Fig. 3.  $\text{Co}_2\text{Si}$ -nanocrystals in 4H-SiC surrounded by onion-like carbon in cross-sectional view projected along  $[11\bar{2}0]$  4H-SiC (a) and in plane-view projected along  $[000\ 1]$  4H-SiC; the insert magnifies the inner part of the onion, showing the nanocrystal (b). The distance between the single shells is 0.34 nm, which corresponds well to the interplanar distance of graphite.

observed in thin specimen areas (as e.g. seen in Figs. 2c, 1a,c and 3a,b) were also found to be surrounded by amorphous materials. Such observation has been made not only for  $\text{Co}_2\text{Si}$  and  $\text{SmSi}_2$  but also in our previous work for the case of  $\text{GeSi}$  and  $\text{ErSi}_2$  nanocrystals [24], however, larger ones were often found to be surrounded by onion-like carbon (see Fig. 3ab) with a mean distance between the shells of  $0.34 \pm 0.03$  nm. The excess of graphite in form of carbon onions in SiC were previously found on laser annealed SiC [38]. The higher mobility of the Si-compared to C-atoms at the high temperature during the laser annealing (estimated 4000 K on top of the surface) was interpreted as the reason for an out-diffusion of Si and the formation of higher local carbon concentrations. Here the carbon excess in the matrix occurs due to the silicide formation of the nanocrystals. At implantation doses near or below  $10^{16} \text{ cm}^{-2}$ , the carbon concentration is not high enough to create onion-like carbon. In analogy to the simple thermal treatment of carbon soot [39], the phase transformation from amorphous carbon to graphite shells observed here may appear after a critical level of carbon concentration is reached.

### 3.2.1. Magnetization measurement by means of electron holography

An electron wave running through an object containing an electric potential  $V$  and a magnetic

field  $\vec{B}$  suffers a phase shift

$$\varphi = 2\pi \frac{e}{h} (V_{\text{proj}}/v + \Phi), \tag{1}$$

with respect to vacuum.  $e$  and  $h$  are electron charge and Planck’s constant, respectively.

$$V_{\text{proj}} = \int_{\text{object}} (V(x, y, z) dz) \tag{2}$$

is the “projected potential” integrated along a trajectory across the object in  $(x, y)$ , and  $v$  is the electron velocity.

$$\Phi = \oint \vec{B}(x, y, z) d\vec{A}, \tag{3}$$

means the magnetic flux enclosed in the area  $\vec{A}$  between the trajectory through  $(x, y)$  and a reference trajectory far away. Examples of spheres with electric potential and magnetized spheres are shown in Fig. 4.

The resulting phase modulation can be evaluated quantitatively by electron holography: the phase-modulated “object exit wave” is superimposed with an unmodulated reference wave by means of the Möllenstedt electron biprism, giving rise to an interference pattern (“hologram”) (Fig. 5). From the hologram both amplitude and phase distribution can be reconstructed by means of numerical image processing for evaluation of electric and magnetic structures in the object; for an overview see Ref. [13]. For our purpose, phase distributions expected for spherical particles are

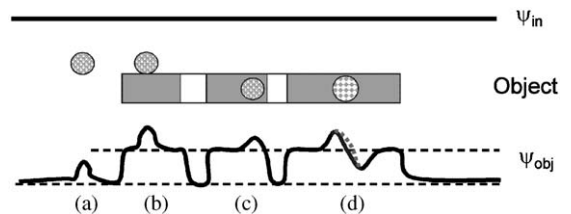


Fig. 4. Scheme how the electron phase of the beam can be affected by different electric and magnetic objects which are either free standing or embedded within a crystal. Electron phase modulation by an electric sphere (a), electric sphere on top of a foil (b), and embedded in a foil (c), separated by holes. (d) shows a sphere homogeneously magnetized perpendicularly to drawing plane without (solid line) and with electric potential (broken line).

presented in Fig. 6. Therefore, in the phase image of magnetized particles, typical structures show up in addition to the electric ones, which reveal the presence of magnetization. A typical phase image is shown in Fig. 7. For determination of the  $\vec{B}$ -field in a sphere, the measured phase shift has to be multiplied by  $\pi/2$  (see Fig. 8).

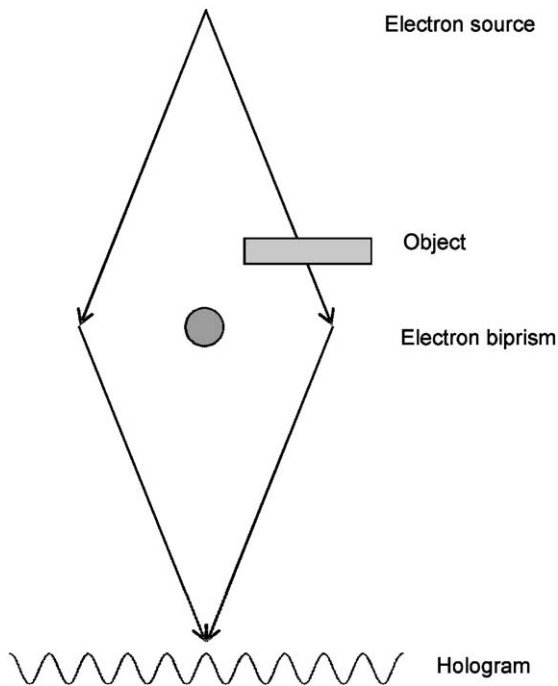


Fig. 5. Scheme for producing an electron hologram. The object wave modulated by the object structure (right) interferes with the plane reference wave (left) to form a hologram.

To investigate the magnetization in a TEM, the environment of the object has to be free from the strong magnetic lens fields, consequently, the objective lens has to be switched off and the so-called Lorentz-lens has to be used instead. Holograms of the Co-particles were taken in this “Lorentz-mode”. The reconstructed phase images reveal magnetic dipoles in nanocrystals created in a sample depth of about 80–100 nm (Fig. 9a). The fields of the magnetic dipoles are randomly oriented, and the typical asymmetric behaviour of the phase of the magnetic dipoles is shown in Fig. 9d, eg. at the nanocrystal marked 2. That the magnetic domains are really caused by nanocrystals can be seen in the standard bright-field image of the same sample area (Fig. 9b) and by HRTEM-images of selected regions (Fig. 9c).

In Table 1 the strengths of the magnetic fields  $B$  caused by the nanocrystals are shown in Fig. 9. The values have been determined by measuring the phase change of the dipoles by using Eqs. (1) and (2).

The strengths of the magnetic field listed in Table 1 ranges between 2 and 4 T. (This order of magnitude shows up for all 20 measured dipoles.)

### 3.3. Co- and Sm-ion implantation

As in the previous two cases, we found that nanocrystals have been formed also after Co/Sm-ion implantation into 4H-SiC and subsequent annealing as can be seen in the tilted bright-field image (obtained in a very thin specimen region) in

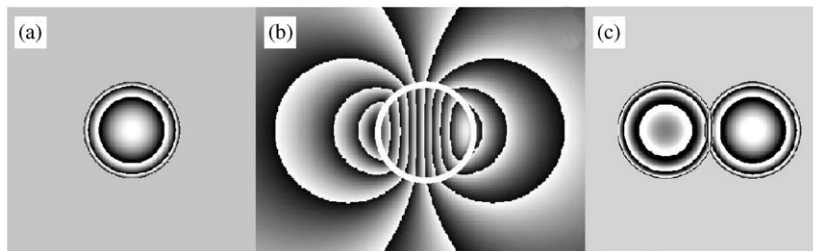


Fig. 6. Simulated phase distributions inside and outside spherical particles with (a) electric potential and (b) inner magnetic field, (c) shows an electric dipole, e.g. given by a sphere close to a hole; this could mimic a magnetized sphere hence lead to misinterpretation. However, in contrast to (c), (b) reveals the typical stray-field reaching far out from the particle, which is characteristic for a magnetized sphere.

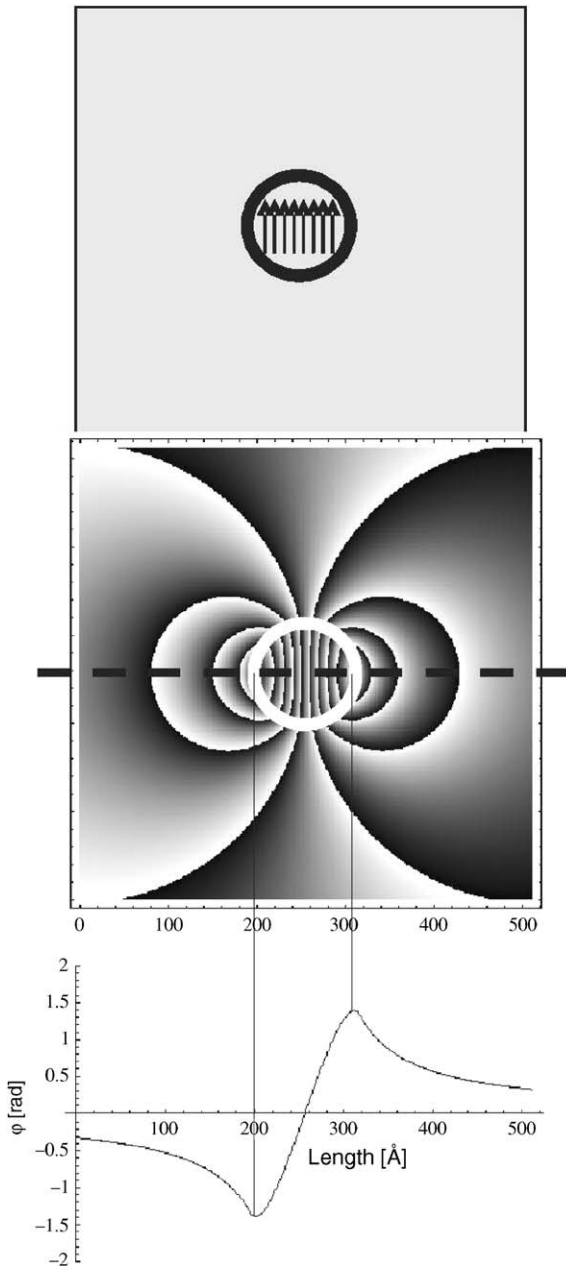


Fig. 7. Simulated phase distribution around a homogeneously magnetized sphere as reconstructed from a hologram. Top: sphere of 30 nm radius with indicated inner magnetic-field of 1 T. Middle: phase distribution with contours. Bottom: linescan of phase along broken line.

Fig. 10a, where the nanocrystals show up dark due to different absorption contrast.

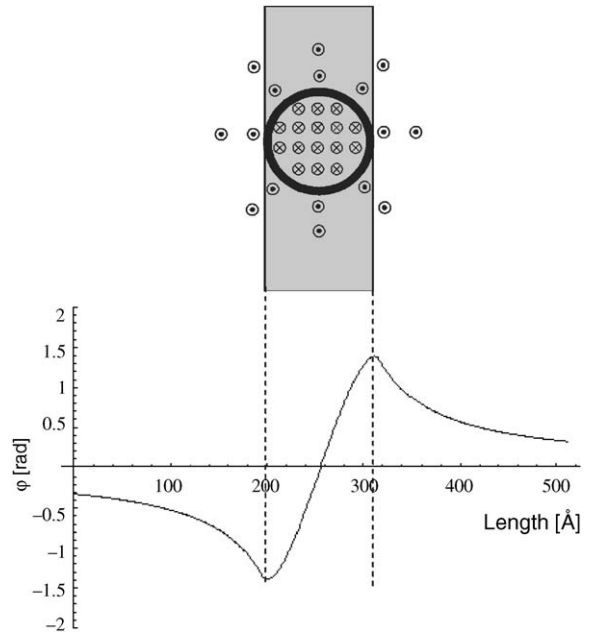


Fig. 8. Evaluation of the inner-field of the sphere from phase distribution. A spherical, single-domain particle is always surrounded by a stray field, which, in the cross-section drawn through the particle center, points in the direction opposite to the inner-field of the particle. Therefore, the magnetic flux enclosed in the grey-shaded area, determining the phase shift, consists of the inner field minus the enclosed stray field. In effect, the stray field reduces the measured phase shift, which would result from the inner-field alone, by a factor of  $2/\pi$ . Therefore, to obtain the inner-field of the particle from the extrema of the measured phase distribution, one has to multiply these values by a factor  $\pi/2$ .

The EDX signals of Sm-and-Co (Fig. 10b) obtained along the arrow marked in Fig. 10a show that both elements have their maximas at about 100 nm, however it can be seen in addition that the distribution of Co is much broader (with TRIM calculated width is 60 nm for 200 keV Co-ions). This leads to a relatively high Co concentration near the surface, but practically no presence of Sm. This is consistent with the fact that the nanocrystals (many of them are half filled voids near the surface are identified from HRTEM images as  $\text{Co}_2\text{Si}$  (see Fig. 11a)). These nanocrystals appear in the orientation- relationship type 1 as also observed for the case of single Co-ion implantation described in Chapter 3.2 (see Fig. 2a). The nanocrystals observed further away

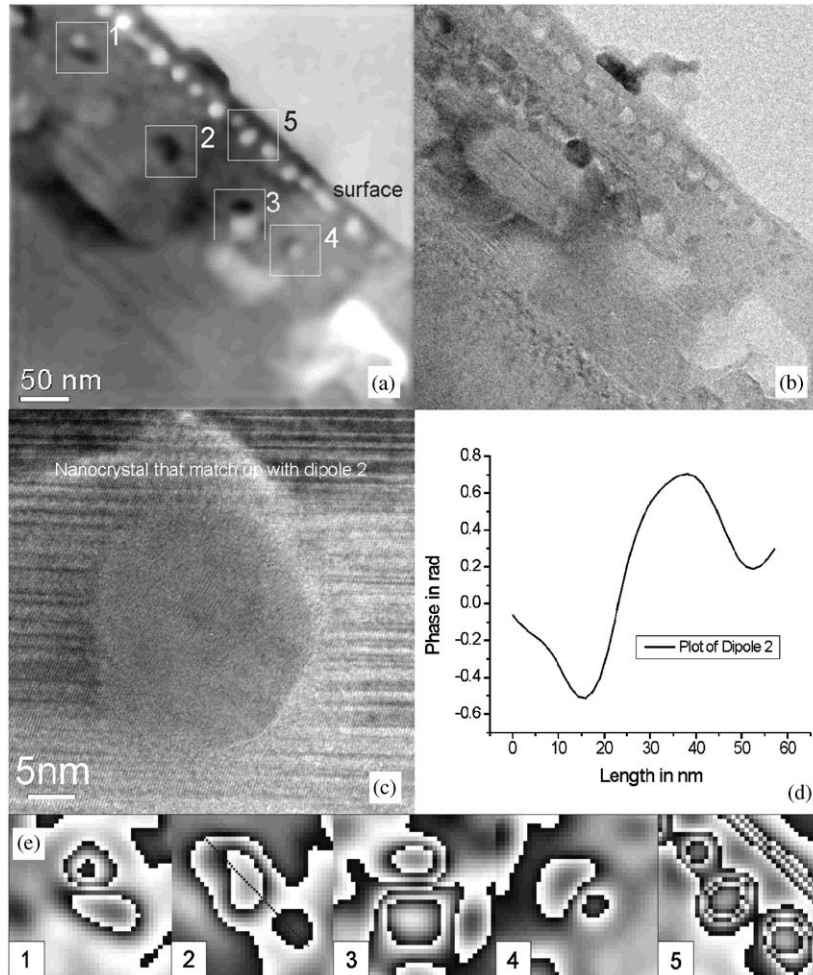


Fig. 9. (a) Reconstructed phase image of Co-ion implanted 4H-SiC. Nanocrystals marked 1–4 show magnetic, those marked 5 electric active behaviour (see (e) compare with Fig. 7). (b) Bright field images showing the same sample area as in (a). (c) HRTEM image of the nanocrystal marked 2. (d) Plot of the phase of the electron wave along region marked 2. The distance of 13 nm between minimum and maximum of phase fits exactly to the diameter of the round shaped nanocrystal 2. (e) Magnified and amplified phase images of the magnetic dipoles marked 1–4 and the monopoles marked 5 in (a), the dotted line in 2 marks the trace of the plot of the dipole shown in (d).

Table 1  
Phase change and strength of the magnetic field of the dipoles marked 1–4 in Fig. 9a

Nanocrystal	$\Delta\phi$ in radiant	$B$ in tesla
1	2.0	4.0
2	1.5	2.0
3	3.2	3.8
4	1.4	3.3

the surface of the sample always shows a more complex crystal structure (Fig. 11b), which could not be identified so far.

The chemical compositions of the nanocrystals in the surface-near region and in the surface-far region (depth about 100 nm, Fig. 11b) have been investigated using EDX- and EELS-STEM-mapping (1.3 nm size of raster, see Fig. 12). The measurements showed that the partly filled voids near the

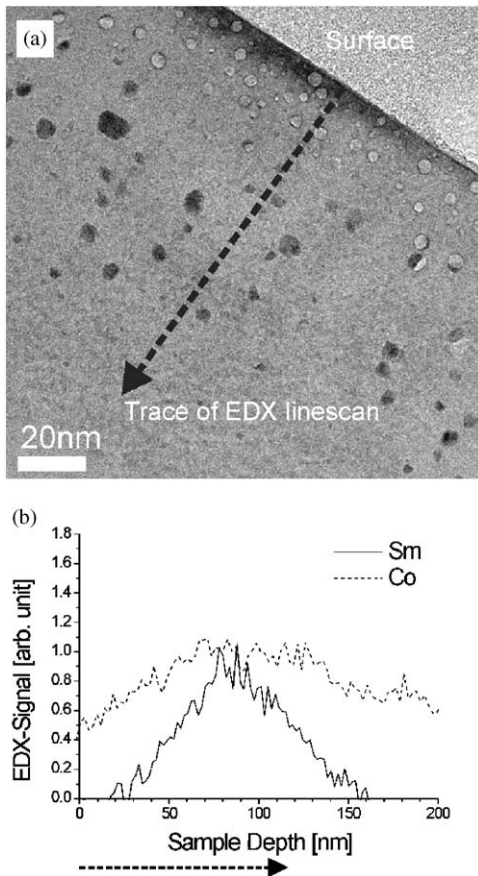


Fig. 10. (a) Bright field image of Sm/Co-ion implanted 4H-SiC. The area selected for EDX-linescan analysis is visualized by the arrow. (b) Element distribution of Co and Sm with maxima at a depth of around 100 nm showing a much broader profile for the case of Co.

surfaces contain Co but not Sm, which agrees well with the averaged element distribution obtained by EDX-linescans (see Fig. 10b) and HRTEM identification of  $\text{Co}_2\text{Si}$ . The surface-far nanocrystals differ (as in the case of Co-ion implantation) from those appearing surface-near. Here they always contain both implanted elements together. Within the detection limit, no Co and Sm were detected in the 4H-SiC matrix. This gives the additional information that most of the implanted atoms are clustered. The Si-signal from the nanocrystals is clearly lower than from the matrix. Therefore the nanocrystals must have a silicon content much lower than 50%, the Si content in SiC (Fig. 12e).

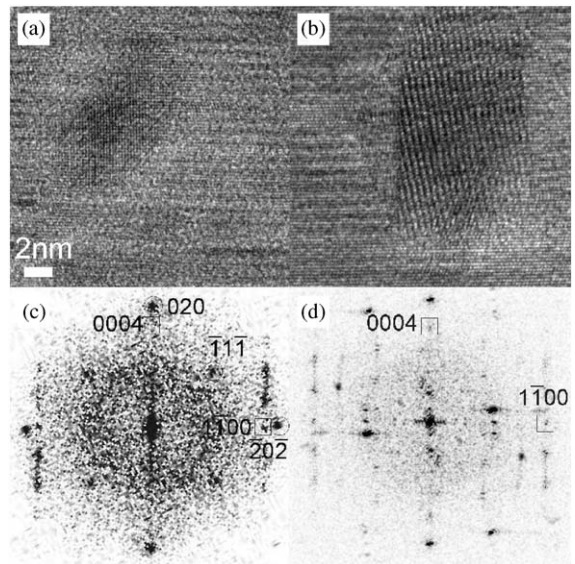


Fig. 11. [11–20] HRTEM images of nanocrystals formed in 4H-SiC after Co/Sm-ion implantation and corresponding diffractograms. (a, c)  $\text{CoSi}_2$ -nanocrystal formed in the surface-near region. (b, d) Nanocrystal of more complex structure formed in the surface-far region. Indexed reflections of nanocrystals are encircled, reflections of 4H-SiC are boxed.

Electron holography on the Co/Sm-ion implanted samples showed no conclusive results so far, which is understandable as the mean size of the nanocrystals corresponds to the resolution limit of Lorentz lens microscopy (about 8 nm). Integral measurements on the Co/Sm-ion implanted samples suggested either a very low magnetization or randomly orientated magnetic domains.

### 3.4. Comparison

When comparing the HRTEM, Z-Contrast (HACDF) and HAADF-EDX/EELS-STEM results of the three implantations into 4H-SiC (Sm, Co and Sm-and-Co), the effect of the different kinds of implanted ions and of the different doses on the size, shape (see Fig. 13), structure, orientation relationship, strain and composition has been evaluated. A total implantation dose of  $10^{16} \text{ cm}^{-2}$  (for the case of Sm-and-Co/Sm-ion implantations) creates nanocrystals with mean sizes of 6–8 nm, the mean size of the empty voids are about half of the

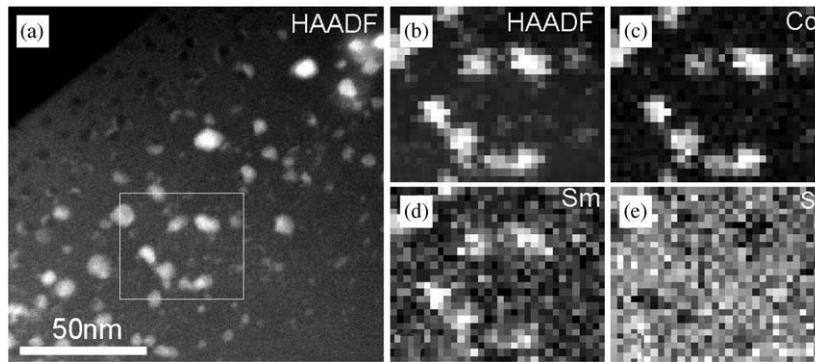


Fig. 12. HAADF-STEM images (a, b) and EDX-STEM maps of nanocrystals created after Co and Sm-ion implantation in 4H-SiC and annealing. (a) overview HAADF-image showing the region (marked) for the EDX-STEM analysis. (b) HAADF-STEM image, (c) Co, (d) Sm and (e) Si-EDX maps (the selected area was scanned with 1.3 nm wide raster). The nanocrystals always show an increase of the Co and the Sm-signal, while the Si-signal in the nanocrystals is clearly lower than in the matrix.

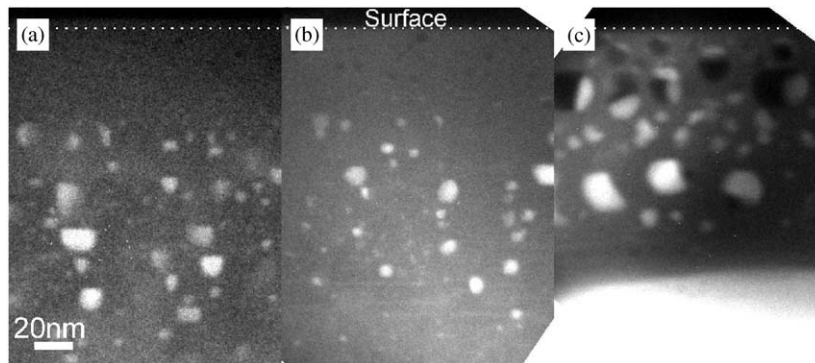


Fig. 13. HACDF-Contrast images (HACDF) of nanocrystals in 4H-SiC formed after (a) Sm (b) Sm/Co (c) Co- ion implantations showing voids and nanocrystals and half-filled voids suggesting that voids are formed everywhere and act as preferred host for nanocrystals. The nanocrystals grow during annealing until every free material is used, leaving empty and half-filled voids. Coalescence of voids and nanocluster leads to bigger objects as seen in (c) where much more ions have been implanted. The dashed line indicates the surface.

mean nanocrystal sizes (2–4 nm) (see Fig. 14). In general, an implantation at 10 times higher dose ( $10^{17} \text{ cm}^{-2}$  Co-ions) should create nanocrystals with two times higher mean sizes (8 times higher volume) if always the same percentage of foreign atoms is clustering. (This was, in fact, experimentally observed comparing the nanocrystal sizes for doses of  $10^{15}$  and  $10^{16} \text{ cm}^{-2}$ , where the nanocrystal mean sizes was 4 and 8 nm, respectively.) Here however the nanocrystals were much larger, up to 40 nm (see Fig. 13c) as at the dose of  $10^{17} \text{ cm}^{-2}$ , nanocrystals (and voids) coalesce. It seems to be reasonable that during the annealing process it is

energetically preferred that the vacancies, matrix atoms and foreign atoms, distributed randomly just after implantation, cluster to voids and nanocrystals, respectively [16,18]. We suggest that the space for the nanocrystal growth in the semiconductor matrix SiC is created when vacancies begin to cluster, therefore these two processes can be linked to each other. The voids are filled, half filled, or empty depending only on the amount of foreign atoms available in the sample depth. Depending on the creation enthalpy, a compound of matrix, and foreign atoms may crystallize as is the case for metal silicides discussed here. The

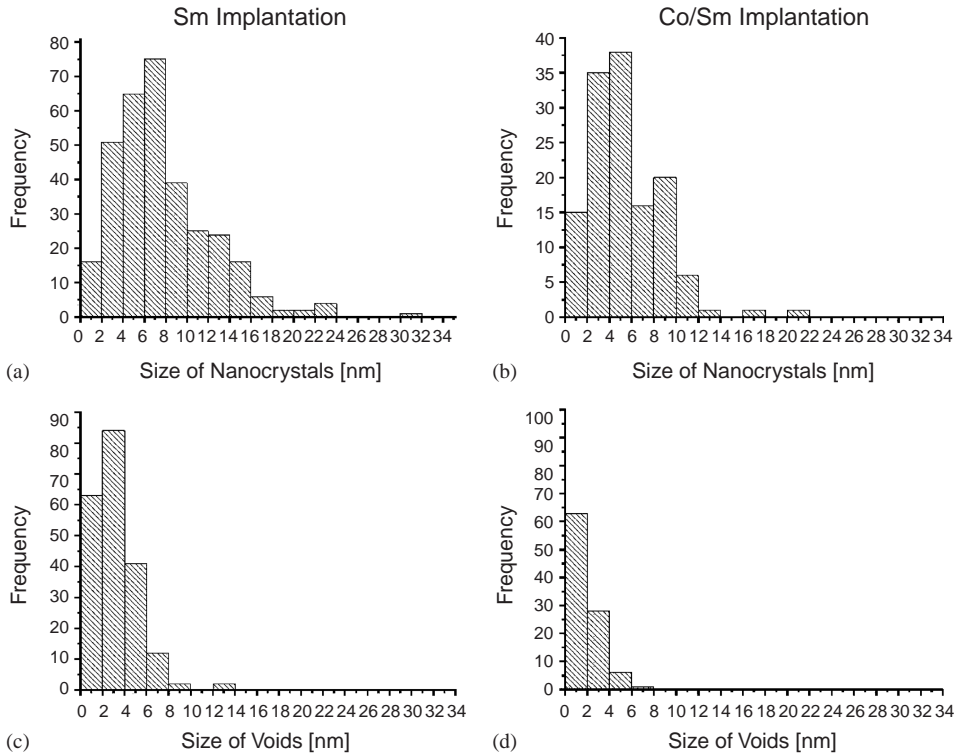


Fig. 14. Size distribution of nanocrystals and matrix voids for the Sm and Co/Sm implantation. It can be easily seen that nanocrystal size are comparable for this two implantations.

resulting excess carbon was found to segregate around the nanocrystals, either as amorphous material or in the form of onion-like carbon, depending on the implantation dose. As the surface is a strong sink for vacancies [40,41] no voids are found on the surface far tail of the Gaussian distribution of foreign atom in the SiC matrix (see the half-filled and empty voids, which appear only near the surface (Figs. 5a and 8)). In the case of the high-dose Co-ion implanted SiC, nanocrystals appear close to the surface due to the large width (60 nm) of the Co-distribution and the high amount of atoms (10% in 100 nm depth).

The Sm-ion implantation creates preferentially nanocrystals of hill-like shapes, which are oriented parallel to the 4H-SiC matrix (type 1a, Fig. 1a). Hill-like shaped nanocrystals in this orientation were observed earlier when ErSi<sub>2</sub> nanocrystals created after Er implantation into SiC [25]. There it was shown that the nanocrystals flip in response

to the SiC-polarity, visualizing clearly that the matrix determines the nanocrystal orientation. Therefore it can be assumed that the SmSi<sub>2</sub> nanocrystals of type 1a form well defined bonds between Sm and the SiC matrix, as was explained for the case of ErSi<sub>2</sub>, resulting in nanocrystals and matrix, which are unstrained (see Fig. 1d). No hill-like shaped but generally faceted and differently oriented nanocrystals which tend to strain the matrix where found after Co and Co/Sm implantation in the depth of maximal foreign atom content. Here the nanocrystals (and not the matrix) dictate the shapes and therefore their orientations (to the connection of shape and orientation relationship see Ref. [24]).

Nanocrystals composed of foreign atoms and Si (silicides) have been formed preferentially. For the case of Sm-ion implantation a few carbide-nanocrystals were found in addition; for the high dose Co-ion implantation a few pure

metal-nanocrystals could be observed. In the region of maximal foreign atom concentration, nanocrystals of more complex structure appear, containing more Co and less (or no) Si (Co-ion implantation) and both kinds of implanted atoms and Si (Co/Sm-ion implantation). No  $\text{SmSi}_2$  and  $\text{Co}_2\text{Si}$  were identified in this depth. It should be mentioned that the formation kinetics of a particular nanocrystal is a rather complex function of the formation enthalpies and defects arrangements on the atomic scale and therefore a spread of possibilities in the nanocrystal structure and composition is reasonable.

Our first measurements of the magnetic properties using both integral methods on the bulk sample (torque magnetometer) and local methods on the single nanocrystals (Lorentz microscopy) revealed ferromagnetism for the case of the Co-ion implantation. Single-domain magnetic nanocrystals clearly show up in the sample depth of the maximum concentration of foreign atoms, surface-near nanocrystals were found to be non-magnetic ( $\text{Co}_2\text{Si}$ ). While the lower dose of the Sm/Co-ion implantation leads to smaller nanocrystals, magnetic domains could not be resolved by Lorentz microscopy. However, as the integral measurements showed a weak magnetic signal it can be concluded that this is caused by randomly aligned magnetic single-domains in analogy to the Co-case. Studies of higher dose Sm-ion and Sm/Co-ion implanted samples are currently being carried out.

#### 4. Conclusion

Preferably foreign atom silicide nanocrystals instead of pure foreign atom nanocrystals have been formed inside 4H-SiC after high dose Sm-, Co- and, Co/Sm-ion implantations and annealing. That means silicon of the matrix is used for silicon compound formation and consequently, carbon is in excess in the matrix. It was shown that excess carbon forms either onion-like or amorphous structures around nanocrystals depending on the implantation doses. As nanocrystals were shown to grow with the implantation dose, adjustable nanocrystal sizes within a semiconductor may be a

future possibility, however their coalescence for the case of very high implantation doses has to be taken into account. Nanocrystals in the depth of maximal foreign atom content are of more complex lattice plane structure (compared to  $\text{Co}_2\text{Si}$  or  $\text{SmSi}_2$  nanocrystals formed surface-near). For those it could be revealed using Lorentz microscopy for the case of Co-implants that they are ferromagnetic and show a magnetic single-domain structure. Their magnetic fields are randomly orientated, which seems to be understandable as also these nanocrystals did not show defined orientation relationships with the matrix, resulting in low signals for the integral measurements. For smaller nanocrystals composed of Sm- and-Co formed after Sm/Co-ion implantation ferromagnetic properties could not be revealed due to the resolution limitation of the Lorentz lens. The ratio of magnetic to non-magnetic nanocrystals is low in the SiC matrix as the stoichiometric silicides were shown to be non-magnetic. Therefore the replacement of SiC by a semiconductor host matrix, where foreign atom silicide nanocrystals formation can be excluded, as diamond or GaN, should be recommended and will be a matter of our future work.

#### Acknowledgements

We are grateful to G. Lenk for ion implantation and to K. Steenbeck for measuring the magnetic properties the samples. This work has been supported by the Deutsche Forschungsgemeinschaft with project Wi 419/9-1.

#### References

- [1] W.J. Choyke, H. Matsunami, G. Pensl, Silicon carbide, Wiley-VCH, Berlin, 1999.
- [2] S. Pokrant, C. Herwig, T. Hihara, J.A. Becker, Eur. Phys. J. D 9 (1996) 509.
- [3] S. Das Sarma, Am. Sci. 89 (1999) 516.
- [4] W.C. Kohler, R.M. Moon, Phys. Rev. Lett. 29 (1972) 1468.
- [5] C. Dufour, K. Dumesnil, S. Soriano, Ph. Mangin, P.J. Brown, A. Stunault, N. Berhhoft, Phys. Rev B. 66 (2002) 094428.

- [6] D.L. Leslie-Pelecky, R.D. Rieke, *Chem. Mater.* 8 (1996) 1770.
- [7] T. Sakai, G. Adachi, T. Yoshida, J. Shiokawa, *J. Chem. Phys.* 75 (6) (1981) 3027.
- [8] L. Pavebi, L. DalNegro, C. Mozzoleni, G. Franco, F. Priolo, *Nature* 408 (2000) 440.
- [9] J. Shi, S. Gider, K. Babcock, D.D. Awschalom, *Met. Semicond. Sci.* 271 (1996) 937.
- [10] V.L. Shaposhnikov, N.A. Sobolev, *J. Phys.: Condens. Matter* 16 (2004) 1.
- [11] M.S. Miao, W.R.L. Lambrecht, *Phys. Rev. B* 68 (2003) 125204.
- [12] N. Theodoropoulou, A.F. Hebard, S.N.G. Chu, M.E. Overberg, C.R. Abernathy, S.J. Pearton, R.G. Wilson, J.M. Zavada, Y.D. Park, *J. Vac. Sci. Technol. A* 20 (3) (2002) 579.
- [13] M. Lehman, H. Lichte, *Microsc. Microanal.* 8 (2002) 447.
- [14] W.V.M. Machado, J.A. Kintop, M.L. De Siqueria, L.G. Ferreira, *Phys. Rev. B* 47 (1993) 13219.
- [15] J. Kim, F. Kirchhoff, J.W. Wilkins, F.S. Khan, *Phys. Rev. Lett.* 84 (2000) 503.
- [16] F. Gao, J.F. Weber, *Phys. Rev. B* 66 (2002) 021406.
- [17] K. Nordlund, R.S. Averback, *Phys. Rev. B* 56 (1997) 2421.
- [18] A. Gali, P. Deak, P. Ordejon, N.T. Son, E. Janzen, W.J. Choyke, *Phys. Rev. B* 68 (2003) 125201.
- [19] A.V. Suvorov, O.J. Lebedev, A.A. Suvorova, J. Van Landuyt, O.I. Usov, *Nucl. Instrum. Methods B* 127/128, 347.
- [20] O.I. Lebedev, G. Van Tendeloo, A.A. Suvorova, I.O. Usov, A.V. Suvorov, HREM study of ion implantation in 6H-SiC at high temperatures, *J. Electron. Microsc.* 46 (1997) 271.
- [21] J. Stoemenos, B. Pecz, V. Herra, *Appl. Phys. Lett.* 74 (1998) 2602.
- [22] U. Kaiser, *J. Electron Microsc.* 50 (2001) 251.
- [23] U. Kaiser, D.A. Muller, J.L. Grazul, A. Chuvilin, M. Kawasaki, *Nature Mater.* 1–2 (2002) 102.
- [24] U. Kaiser, J. Biskupek, D.A. Muller, K. Gärtner, Ch. Schubert, *Crys. Res. Tech.* 37 (2002) 391.
- [25] U. Kaiser, D.A. Muller, A. Chuvilin, G. Pasold, W. Witthuhn, *Microsc. Microanal.* 10 (2) (2004) 303.
- [26] T. Gorelik, U. Kaiser, Ch. Schubert, W. Wesch, U. Glatzel, *J. Mater. Res.* 17 (2002) 479.
- [27] J.P. Biersack, J.F. Ziegler, *The Stopping and Ranges of Ions in Matter*, vol. 1, Pergamon Press, Oxford, 1996.
- [28] Ch. Schubert, U. Kaiser, T. Gorelik, A. Hedler, J. Kräußlich, B. Wunderlich, G. Heß, K. Goetz, U. Glatzel, W. Wesch, *J. Appl. Phys.* 91 (2002) 1520.
- [29] G. Radnoczi, A. Barna, *Surf. Coat. Technol.* 80 (1996) 89.
- [30] U. Kaiser, A. Chuvilin, *Microsc. and Microanal.* 9 (2003) 36.
- [31] E. Voelkl, L.F. Allard, B. Frost, *J. Microsc.* 180 (1995) 39.
- [32] W.J. de Ruijter, R. Sharma, M.C. McCartney, D.J. Smith, *Ultramicroscopy* 57 (1995) 409.
- [33] M.J. Hÿtch, *Microsc. Microanal. Microstruct.* 8 (1997) 41.
- [34] A. Rosenauer, S. Kaiser, T. Reisinger, J. Zweck, W. Gebhardt, D. Gerthsen, *Optik* 102 (1996) 63.
- [35] J. Biskupek, U. Kaiser, *J. Electron Microsc.* 53 (6) (2004) 601.
- [36] A. Chuvilin, U. Kaiser, *Ultramicroscopy* (2005), accepted.
- [37] U. Kaiser, J. Biskupek, K. Gärtner, *Philos. Mag. Lett.* 83 (2003) 253.
- [38] T. Gorelik, S. Urban, F. Falk, U. Kaiser, U. Glatzel, *Chem. Phys. Lett.* 373 (2003) 642.
- [39] W.A. de Heer, D. Ugarte, *Chem. Phys. Lett.* 207 (1993) 480.
- [40] P.F. Fahey, P.B. Griffin, J.D. Plummer, *Rev. Mod. Phys.* 61 (1989) 289.
- [41] H. Rÿcker, B. Heinemann, R. Kurps, *Phys. Rev. B* 64 (2001) 073202.